

Supporting Information

**Radiofrequency-Triggered Surface-Heated Laser-Induced Graphene Membranes for Enhanced
Membrane Distillation**

Hasib Mahbub,¹ Fouzia Hasan Nowrin,¹ Mohammad A. Saed,² Mahdi Malmali^{1}*

*¹Department of Chemical Engineering, Texas Tech University, Lubbock, Texas 79409, United
States*

*²Department of Electrical & Computer Engineering, Texas Tech University, Lubbock, Texas
79409, United States*

**Corresponding author email address: mahdi.malmali@ttu.edu; Tel.: (806) 834-8706; Fax:
(806) 742-3552*

Number of pages: 24

Number of figures: 17

Number of tables: 3

Number of videos: 2

S1. Materials Fabrication and Characterization

S1.1: PES Membrane Substrates Fabrication

Substrates were fabricated via non-solvent induced phase separation (NIPS) technique, using NMP as the solvent and DI water as the non-solvent in the coagulation bath. PES powder was dried first at 80 °C for 24 h before use to remove any residual moisture. Step-by-step fabrication process of the membrane is shown in Figure 1a. Polymer dope solution was prepared with 16, 18, 20, and 22 wt.% PES for this work. First, PES was added to NMP, and the solution was stirred at 70 °C for approximately 6 h until a homogeneous solution was obtained. Then the solution was left at room temperature for 24 h to remove any air bubbles present. Afterward, the solution was spread over a smooth and clean glass plate using a casting knife film applicator (Gardco) operated by an automatic drawdown machine (3.5 inches per second speed and 3.5 inches stroke length) with a gauge height of 700 μ m. Then, the glass plate was transferred to the coagulation bath. After 30 min, the membrane was removed from the coagulation bath and placed in fresh DI water for 24 h to complete the phase separation. Subsequently, the wetted membrane was immersed in 10 wt.% CaCl_2 bath for 1 h. The membrane was removed from the CaCl_2 solution and dried in a convection oven (Binder FD 23 – UL) at 50 °C for 48 h. Membranes prepared with different PES concentrations are denoted as PES-LIG-16 (16 wt.%), PES-LIG-18 (18 wt.%), PES-LIG-20 (20 wt.%), and PES-LIG-22 (22 wt.%), respectively.

S1.2: CO_2 Lasing

The surface of the prepared PES membrane was modified with the laser ablation process to fabricate the hydrophobic surface using a vector mode laser template. PES membranes with casting thickness of 700 μ m were irradiated with a 10.6 μ m CO_2 laser system (Universal Laser System VLS 3.6, 40 W) in the ambient condition. A cross-hatch pattern with a spacing of 1/72" was used to form hydrophobic LIG surface. Adobe Illustrator graphic software was used to make the template keeping interline spacing of 1/72" and line width of 0.001 pt in the graphic software. Then the template was sent for printing to the laser machine where the laser head followed the pattern on the substrate surface. Laser power varied from 1% to 14% with an increment of 1%. All the PES membrane substrates lased in this work were ablated with hatch pattern:1/72", speed:40% and PPI:1000. The selection of the laser power (ranging from 1-14%) was based on the

concentration of polymer dope. Laser power was gradually increased until the laser burnt through the membrane.

S1.3: Characterization

Scanning electron microscope (SEM) images for the surface and cross-section of the membranes were taken with field-emission scanning electron microscopy (S-4700, Hitachi, Japan). Each sample was coated with gold and palladium alloy in a sputter coater. Energy-dispersive X-ray spectroscopy (EDS) mapping was carried out using EDAX (Mahwah, NJ) Phoenix X-ray analyzer equipped with an ultrathin window attached to the Hitachi S- 4700 SEM. Surface hydrophobicity for the membrane samples at different laser power was studied by measuring the equilibrium and dynamic water contact angle using the sessile drop and tilted drop technique, respectively, with KRÜSS DSA30S (KRÜSS, Germany). Raman spectra were taken with SENTERRA dispersive Raman microscope spectrometer (Bruker Optics). PES-LIG membrane film was not directly used for Raman analysis as it can capture signal from the PES between the lines of the cross-hatch pattern. Hence, graphene was scrapped from the membrane surface. However, scrapping the stable graphene was still difficult as PES also got scrapped with LIG, which eventually contributed to noise in the spectrum. At least twenty square inches of the sample was scraped to collect 5 mg of graphene. Transmission electron microscopy (TEM) images were captured using a Hitachi H-9500 transmission electron microscope with a laser wavelength of 532 nm. X-ray photoelectron spectroscopy (XPS) analysis was performed using a Physical Electronics PHI 5000 VersaProbe II with a beam size of 50 μm and a take-off angle of 45°. The spectra were calibrated using C1s at 284.5 eV. The pore size distribution of the membrane was measured by Brunauer–Emmett–Teller (BET) analysis using a micromeritics® 3Flex analyzer (Norcross, GA) with vacuum degassing for 10 h at 130 °C. PES-LIG membranes were cut into small pieces and used altogether in the sample holder for the BET test. Thermogravimetric analysis (TGA) was conducted using an TGA-I 1000 (Instrument Specialists Incorporated, WI) to study the thermal stability of the membranes under nitrogen flow at a heating rate of 10 °C/min from 25 to 800 °C. The tensile tests were conducted using a UniVert mechanical tester (CellScale Biomaterial Testing, Canada). The measurements were taken at 25 °C with a constant crosshead speed of 10 mm/min.

SI.4: RF heating

The heating performance of the LIG samples was studied using an RF power source supplied by a signal generator SRS SG384. Schematic of the RF heating setup is shown in Figure S1a. The signal generator output was supplied to the input of an RF amplifier (Amplifier Research, model 500W1000A - Souderton, PA). The amplifier output was connected to a non-contact fringing field RF applicator using a 50-ohm coaxial transmission line. The RF applicator was made of copper tape and was directly connected to a Type N bulkhead connector. The applicator was designed with a geometry that can fit on the permeate side of the MD module. Schematic of the RF applicator is shown in Figure S1b. Reflection coefficient measurement experiments were carried out to find the frequency that can result in minimal signal loss with the help of Agilent Technologies E5071C network analyzer in the RF frequency range of 50 – 350 MHz. Figure S1c shows schematic of the setup for the reflection coefficient measurements.

The membrane LIG surface was facing toward the feed water circulation, while the non LIG surface was in contact with the applicator inside the membrane cell. Three different frequencies of 91, 150, and 200 MHz were selected and evaluated for MD tests. RF input power to the heater was varied by controlling amplifier gain from 0% to 20%. To calculate the input power, reflection coefficient was calculated by calibrating the end terminal of the 50Ω coaxial cable where the membrane module with RF heating applicator was connected for surface heating VMD test. The reflection coefficient for the membrane samples was then measured, which provided accurate information about the percentage of the incident power that's reflected from the sample and applicator. The power delivered to the applicator was then calculated using Equation 1 below.

$$P_{input} = (1 - |\Gamma|^2) \times P_{FWD} \quad (1)$$

where,

P_{input} = input power to the heater (delivered power)

Γ = reflection coefficient

P_{FWD} = forward power (incident power)

RF field was applied at ambient condition for all the experiments reported in this work. The heating response of membranes at different RF settings was recorded using an A300-Series FLIR thermal camera. For the cyclic thermal stability test, LIG membranes were placed over the applicator and

exposed to RF field with consecutive 15-min heating cycles, followed by 5-min cooling cycles with the RF field turned off. One complete cycle is comprised of one heating and one cooling step, and a total of 20 cycles were performed.

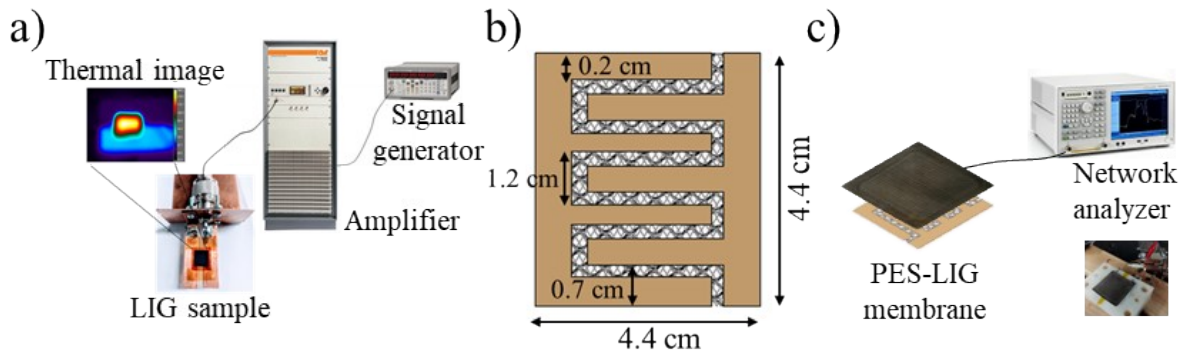


Figure S1. a) Schematic of RF heating apparatus. b) Schematic of reflection coefficient measurement setup. (Inset: PES-LIG membrane placed on membrane module) c) Schematic of the applicator used for RF heating.

SI.5: VMD experimental setup

A schematic diagram of the RF heated VMD setup used in our work is shown in Figure S8. 2 g/L NaCl solution was used as feed for the experiments. The feed flow rate was varied from 3.45 to 30 L/h to the membrane cell using a peristaltic pump which was measured using an Entegris Accutek® flowmeter (Billerica, MA). Custom designed tank with a 2 L capacity made of cast nylon tube was used as the feed tank. The feed tank level was maintained with the help of a level controller that actuates the makeup water pump to deliver water from the makeup tank to the feed tank. The makeup tank was placed on a balance, and changes in the weight were recorded to calculate the flux. The membrane cell was made of Delrin, having a rectangular chamber on both the feed and permeate sides. The RF applicator was placed under the membrane and sandwiched between the module chambers. The RF applicator was connected to RF amplifier using a 50Ω coaxial cable. The signal generator was used as the RF source, which was connected to the input of the RF amplifier. The active area in the module was 21 cm^2 . A diaphragm vacuum pump (WELCH, USA) was used to maintain permeate pressure to 26.5 inHg. Permeate vapor was condensed with the help of a cold trap, and conductivity was measured at the end of the experiment by collecting the permeate water except for the long-term experiment, which was collected continuously. Operating conditions like RF amplifier gain, frequency, were varied to find optimum

performance of the membrane. Weight difference of the makeup tank was recorded to calculate the vapor flux.

The water vapor flux (J) of the membrane and salt rejection rate (R) was calculated using the following equations.

$$J = \frac{\Delta w}{A \times t} \quad (2)$$

Where J is the vapor flux of water, Δw (kg) is the weight of the makeup feed injected at each time interval; A (m^2) is the active membrane area; t (h) is the time interval between each injection.

$$R = \left(1 - \frac{C_d}{C_f}\right) \times 100 \quad (3)$$

Where C_f and C_d are the salt concentration of the feed and distillate, respectively.

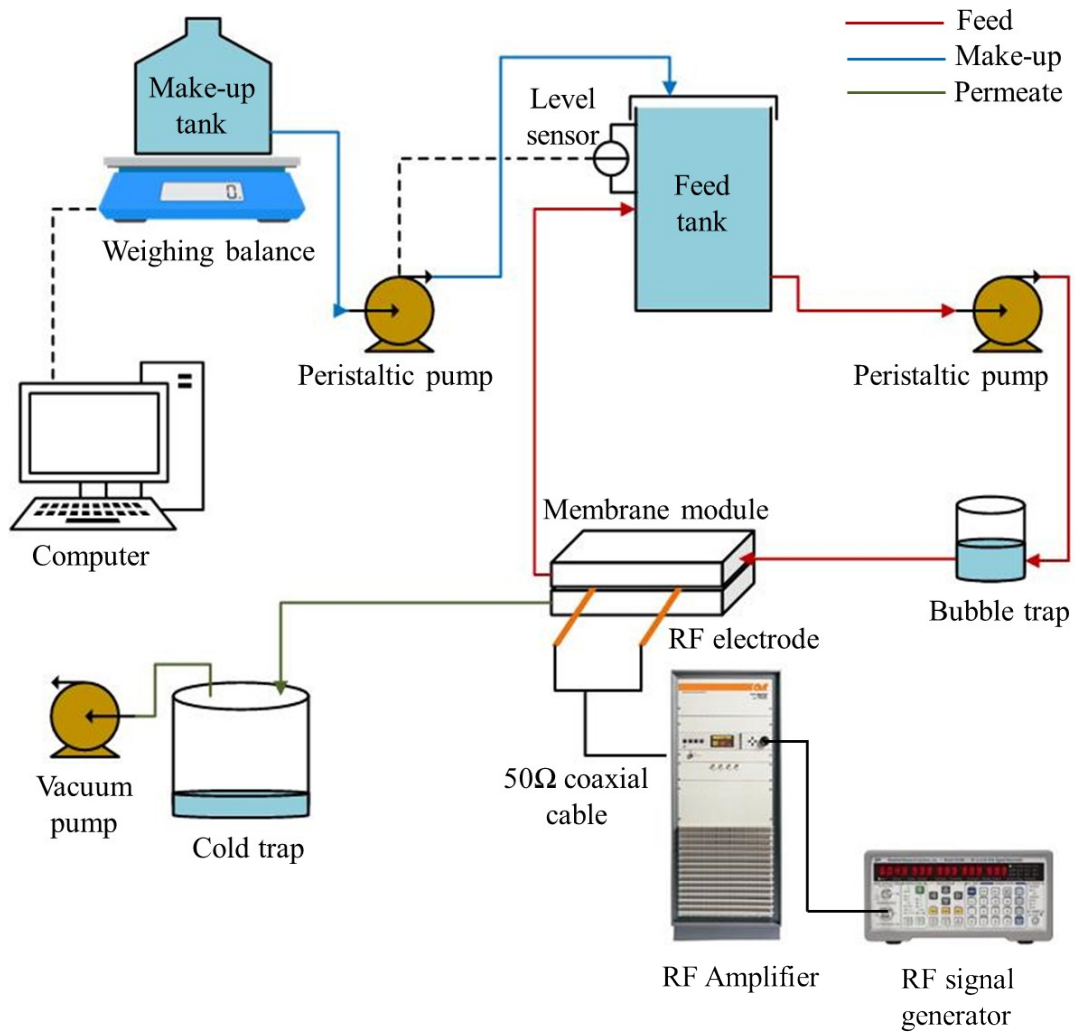


Figure S2. Schematic of lab scale RF heating VMD setup.

S2. Mechanism of LIG formation from PES membrane substrate

In laser irradiation technique, the target substrate material absorbs incident energy within a short time which creates high localized temperature.^[1] Since the time for dissipation of this heat energy is insufficient, this induces photothermal reaction that converts the substrate into porous graphene by converting the sp^3 carbon atoms to sp^2 carbon atoms.^[2] This conversion takes place by breaking the covalent bonds of the functional groups in the substrate which is mostly released as gas. The remaining aromatic compounds rearrange to form graphene structures.

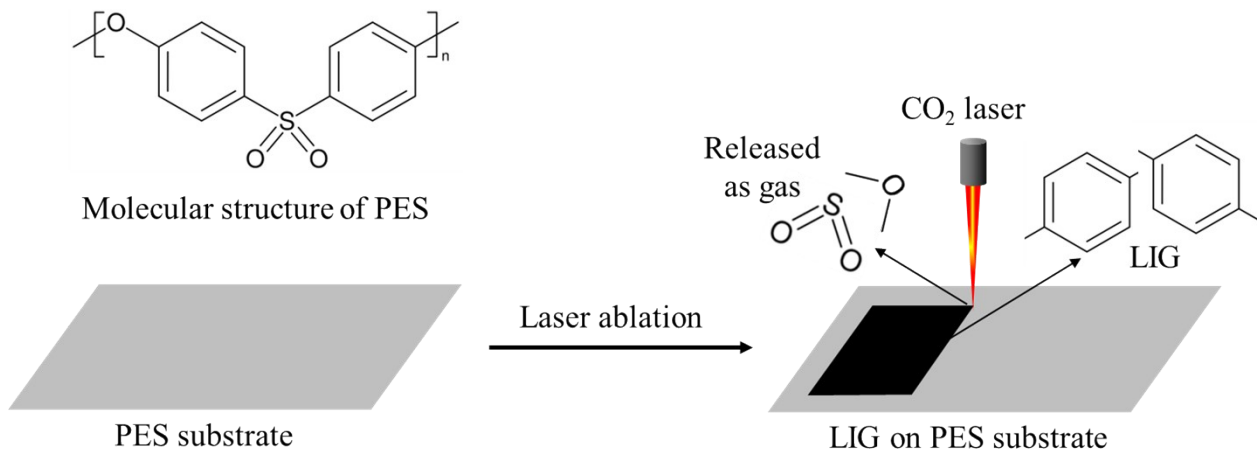


Figure S3. Mechanism of LIG formation from PES membrane substrate under laser ablation, converting sp^3 carbon to sp^2 carbons.

S3. Laser Scanning: Raster and Vector mode

A typical laser machine operates in two different modes of laser scanning: raster and vector. In the raster mode laser ablation, the laser head moves left to right or right to left (along x axis). This mode prints on the surface of the substrate from a pixel based graphic template. In the vector mode, laser head moves along both x and y axes, which print only vector graphics that are composed of paths or lines. Raster mode lasing is affected by laser parameters like power, speed, PPI, and LPI. Vector mode lasing is also affected by power, speed, and PPI; however, LPI has no significant effect as in the vector mode, laser head moves along the paths of the graphic template used for printing. Role of LPI and PPI in laser ablation is shown in Figure S1. LPI controls the number of laser lines passing perpendicular to the y axis, as displayed in Figure S1a. This indicates that LPI is only effective for laser head movement in the x direction, which is the case in raster mode lasing. PPI, on the other hand controls the number of laser pulses per unit length along the laser head movement, x axis for the raster mode and both x and y axes for the vector mode lasing. Increasing PPI decreases inter-distance between two consecutive laser pulses along the direction of laser head movement, as illustrated in Figure S1b.

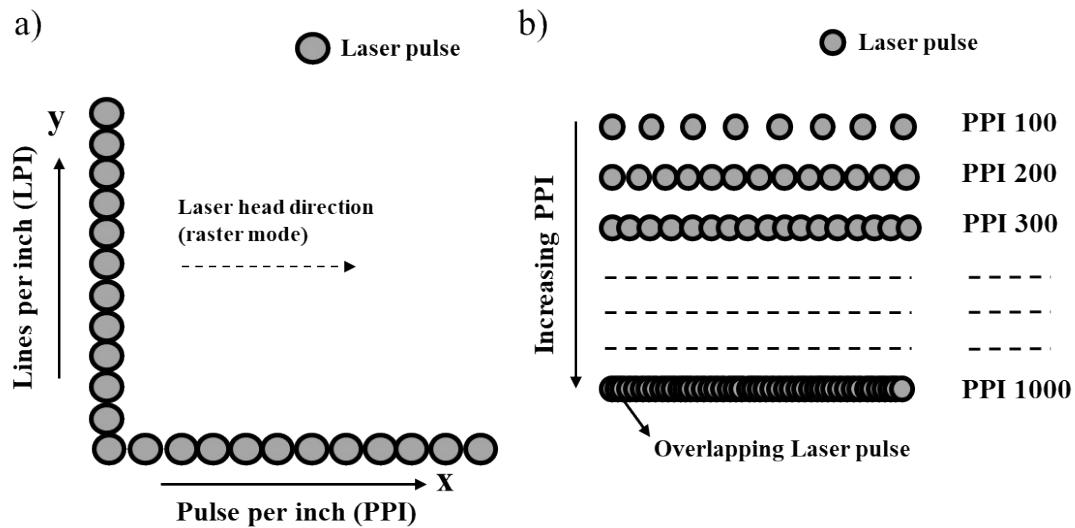


Figure S4. Schematic diagram of the effects of a) LPI and b) PPI.^[3]

S4. Contact angle and SEM analysis of PES-LIG-16 and PES-LIG-20 membrane

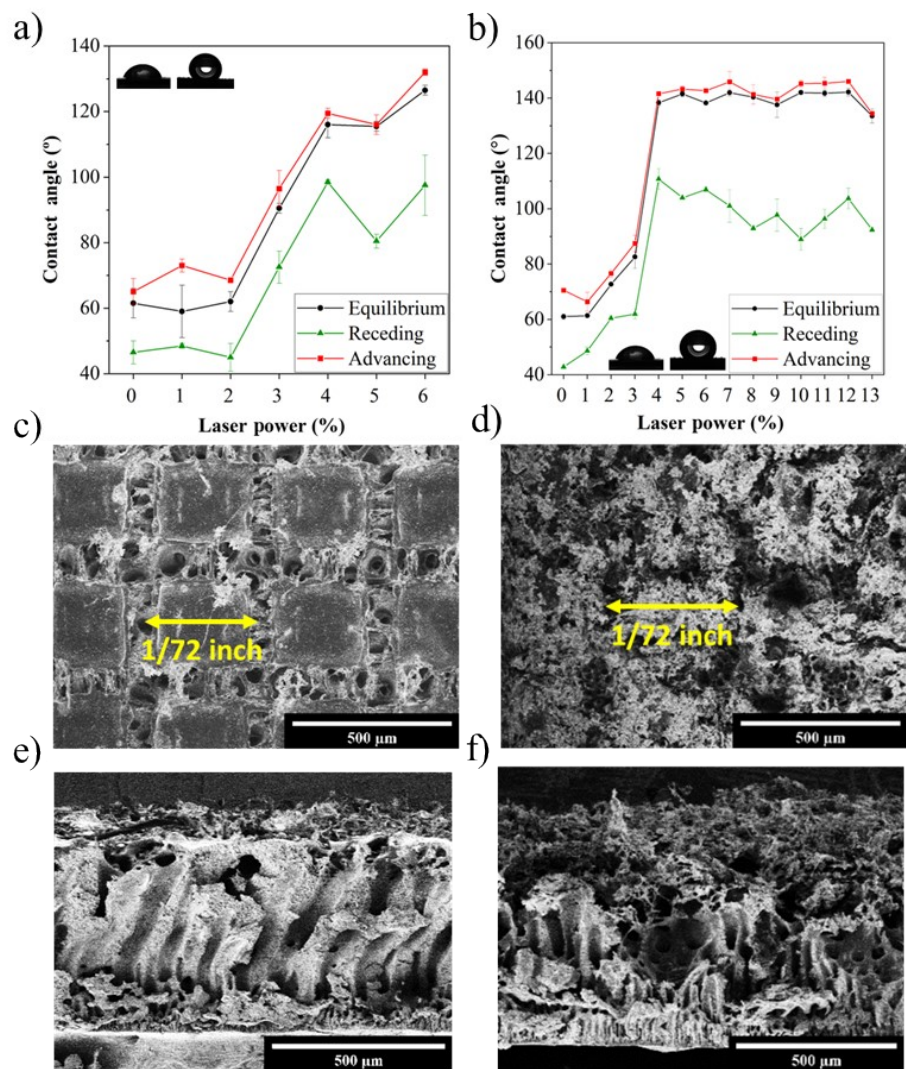


Figure S5. a) Contact angle of PES-LIG-16, and b) PES-LIG-20 PES membranes. SEM surface and cross-section images of c, e) PES-LIG-16, and d, f) PES-LIG-20 PES membranes, respectively.

S5. PES membrane after laser ablation at different laser power

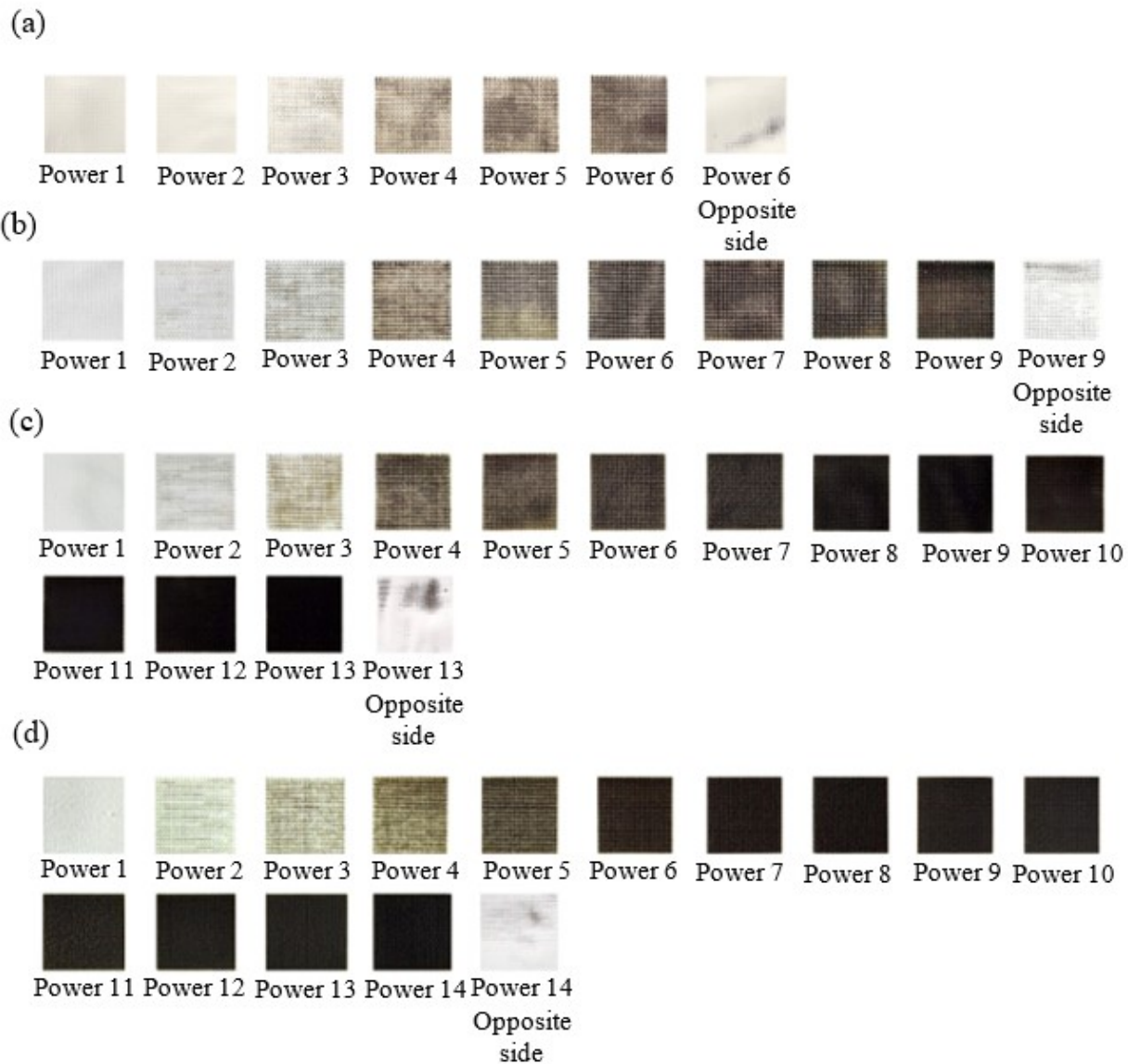


Figure S6. Digital images of a) PES-LIG-16, b) PES-LIG-18, c) PES-LIG-20, and d) PES-LIG-22 membranes at different laser powers.

S6. Lasing surface selection of the membrane

Polymer membranes prepared using the phase inversion technique are asymmetric in structure, having a thin nonporous layer on a much thicker layer with a finger-like porous structure. For further discussion, we will refer to the thin nanoporous layer as the front side and the thicker layer as the back side of the membrane.

In the LIG ablation technique, high temperature at the laser pulse and PES-LIG membrane contact point converts the PES to graphene (Section 2.1). However, nearby areas of the laser contact point at the membrane surface have relatively lower temperatures that cannot graphitize. This temperature is high enough to melt the polymer, though. In Video S1, we showed that lower power can cause membrane melting without producing graphene. This melting of the polymer deteriorates the membrane's porous structure, compromising the membrane's performance. The front side of our PES-LIG membrane has smaller pores that get clogged due to melting under laser ablation. Figure S5a shows the SEM cross-section image of a PES-LIG-18 membrane lased on the front. Compared to the SEM cross-section image of the similar membrane lased on the back (Figure 3b), Figure S5a shows collapsed porous structure due to the melting of the polymer.

Comparison of VMD performance and the LIG surface water contact angle of the PES-LIG membranes is also shown in Figure S5b. A significant difference in the contact angle was not observed for the front and back side lasing. However, for all four membranes, the permeate flux increased by eightfold with membranes lased on the back. Based on this observation, we selected the back of the membrane as the lasing surface to synthesize PES-LIG membranes.

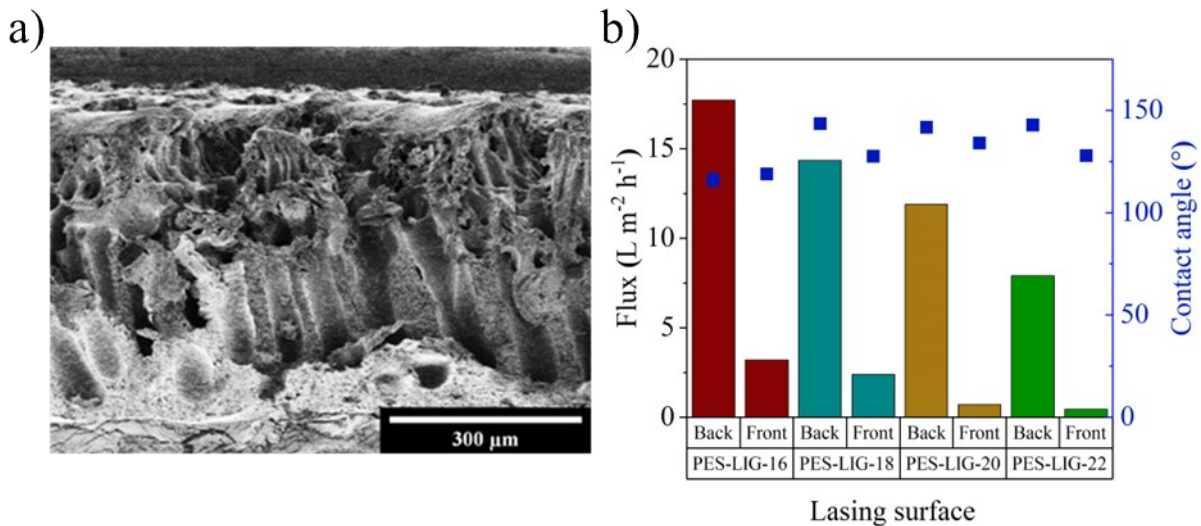


Figure S7. a) SEM cross-section image of PES-LIG-18 membrane with LIG on the front, and b) Flux and contact angle comparison for the PES-LIG-16, PES-LIG-18, PES-LIG-20, and PES-LIG-22 membrane lasing on the back and front side. Laser Setting- speed: 40, PPI: 1000. Note: The flux data reported here are based on evaluating LIG membranes in the conventional MD mode (feed temperature: 50 °C, permeate pressure: 26.5 inHg, flow rate: 30 L/h)

S7. Optimized laser power

Table S1. Optimized laser power for LIG-PES membranes of different polymer concentrations.

Membrane	Optimized laser power (%)
PES-LIG-16	4
PES-LIG-18	7
PES-LIG-20	10
PES-LIG-22	11

S8. CaCl_2 untreated PES membrane under laser treatment

Laser treatment for the membranes made in this work without CaCl_2 treatment was done to prove the role of CaCl_2 in protecting the porous structure of the membranes. PES membranes without CaCl_2 treatment were laser ablated with optimum laser power (Table S1). Figure S5 shows the digital images of both sides of the samples after lasing, which are burnt partially or completely, leaving defects on the membrane. This proves that PES membranes without CaCl_2 treatment cannot be used for laser writing with relatively higher laser power and cannot be used for desalination applications.

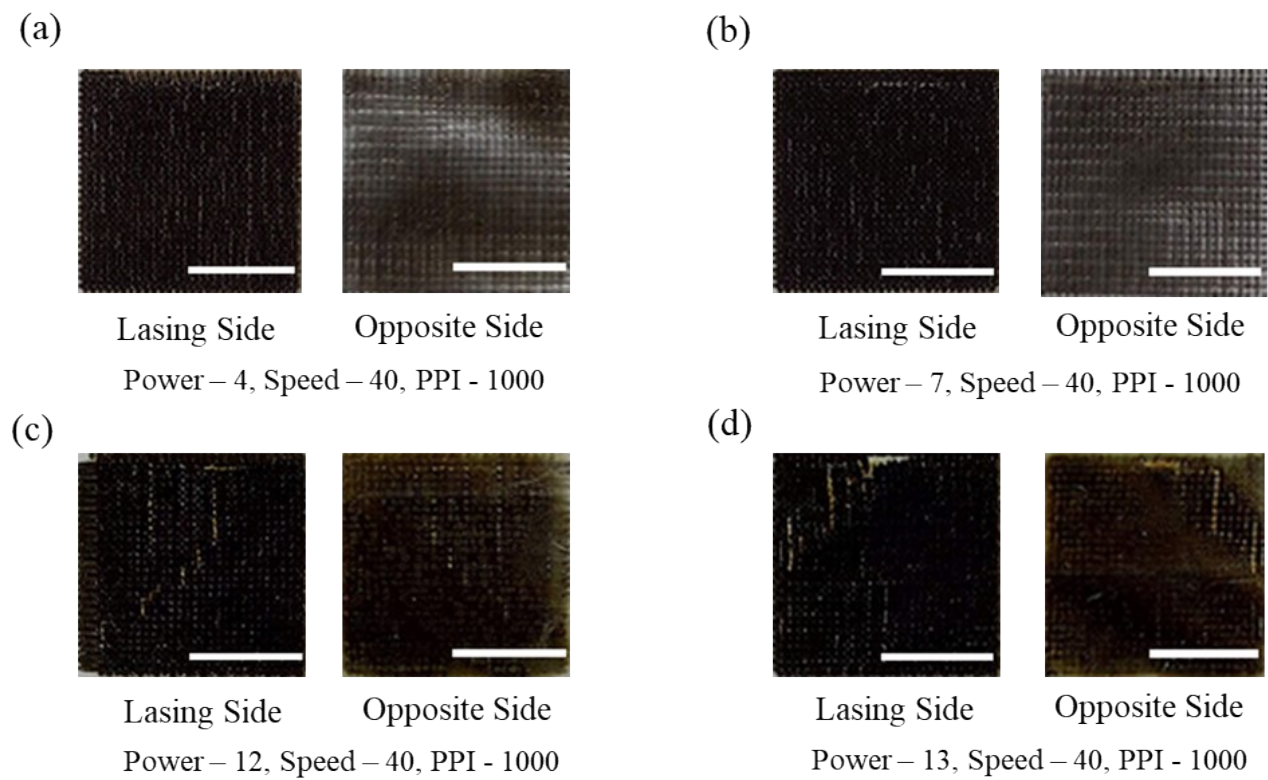


Figure S8. a) PES-LIG-16, b) PES-LIG-18, c) PES-LIG-20, and d) PES-LIG-22 membranes without CaCl_2 treatment after lasing with optimized laser settings (Table S1). (Scale bar – 5 mm)

S9. EDS mapping of Cl atom

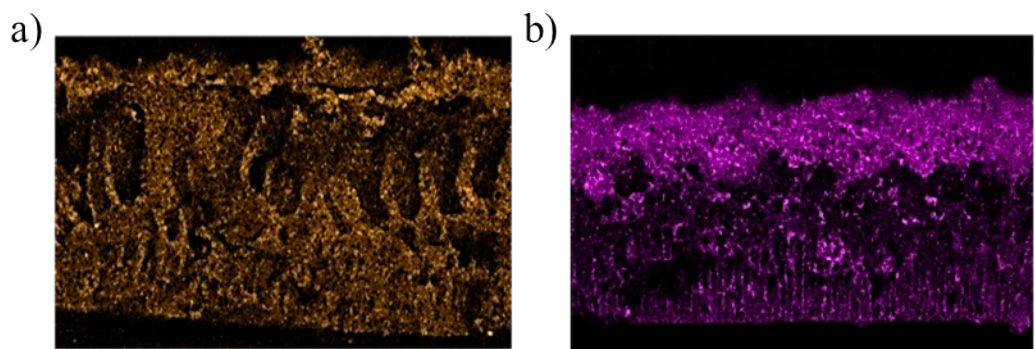


Figure S9. EDS mapping of Cl in the cross section of a) PES-LIG-18, and b) PES-LIG-22 membrane. Laser setting- a) power: 7, speed: 40, and PPI 1000. b) power: 11, speed: 40, and PPI 1000.

S10. Atomic composition from XPS survey spectra**Table S2.** Atomic composition from XPS survey spectra of PES and LIG region from PES-LIG-22 membrane.

Element	Atomic composition (%)	
	PES	LIG
C1s	76.7	87.1
O1s	11.7	9.2
S2p	5.7	2.3
Cl2p	3.0	0.9
Ca2p	3.0	0.5

S11. XPS high resolution spectra of PES membrane substrate

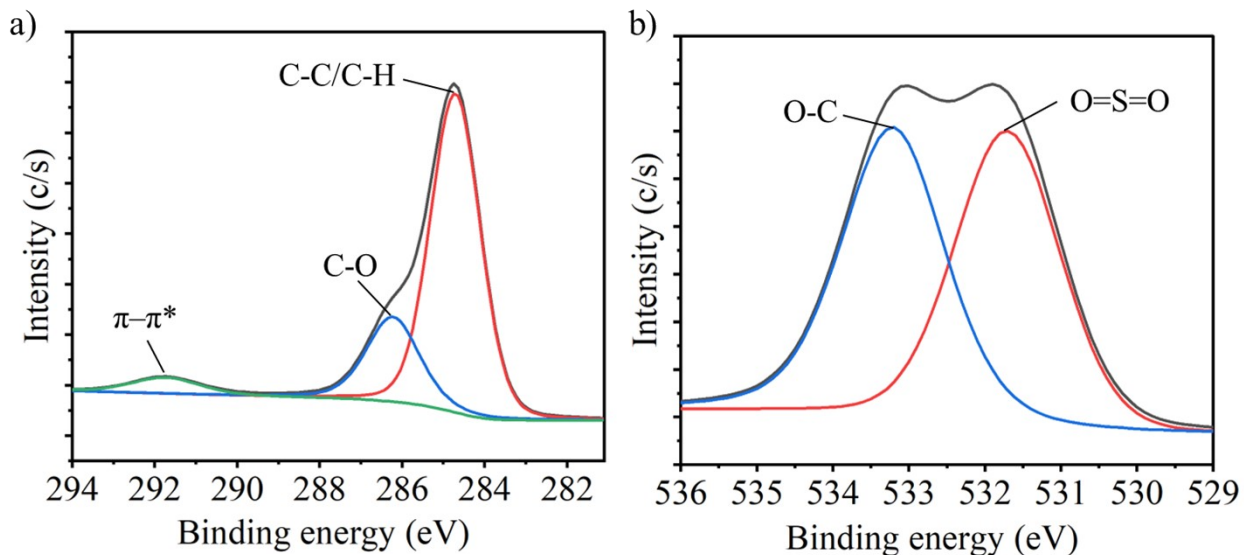


Figure S10. a) C1s, and b) O1s high-resolution spectra of PES portion of PES-LIG-22 membrane.

S12. Pore size distribution of PES membrane substrate

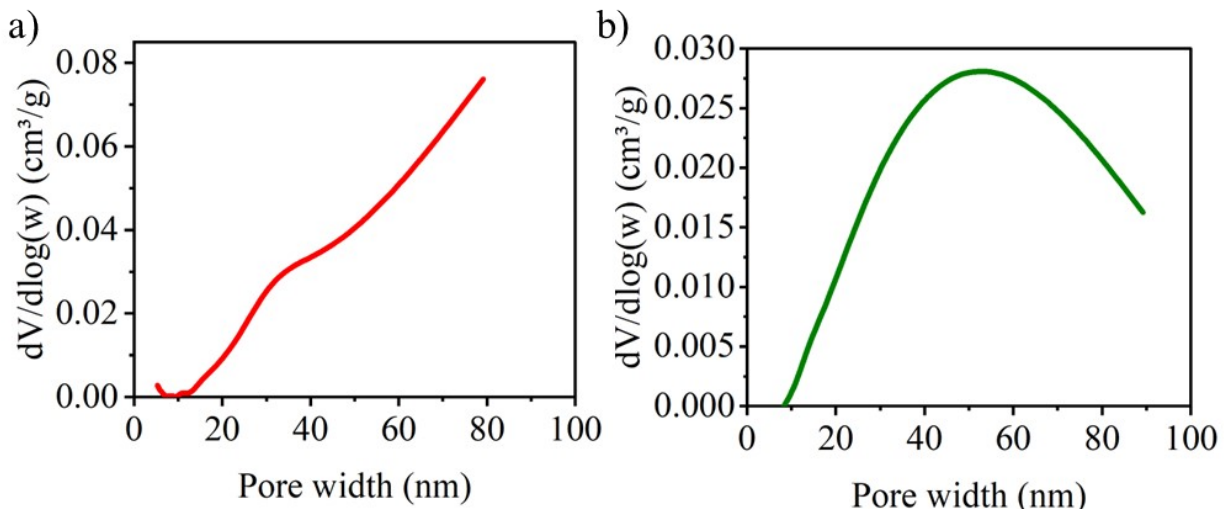


Figure S11. Pore size distribution of a) 18%, and b) 22% PES membrane substrate.

Table S3. BET pore volume and surface area of PES and PES-LIG membranes.

Sample	Pore volume (cm ³ /g)	Surface area (m ² /g)
18% PES membrane substrate	0.06	4.95
PES-LIG-18	1.35	5.9

22% PES membrane substrate	0.043	2.7
PES-LIG-22	0.65	2.8

S13. TGA analysis of PES membrane substrate

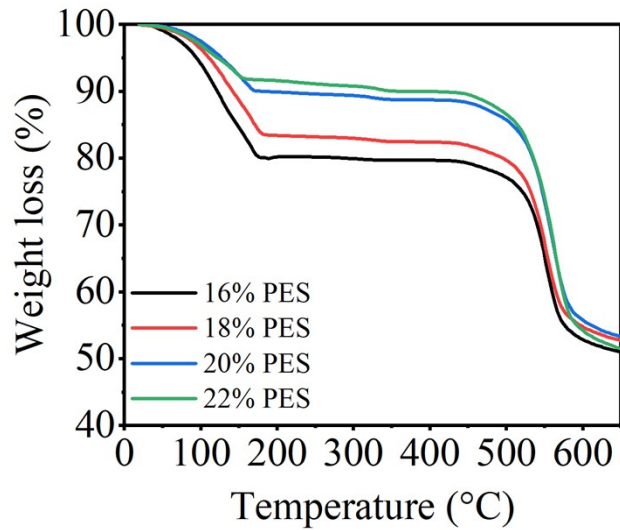


Figure S12. TGA analysis of PES membrane substrate without any LIG.

S14. Example FLIR image of thermal response

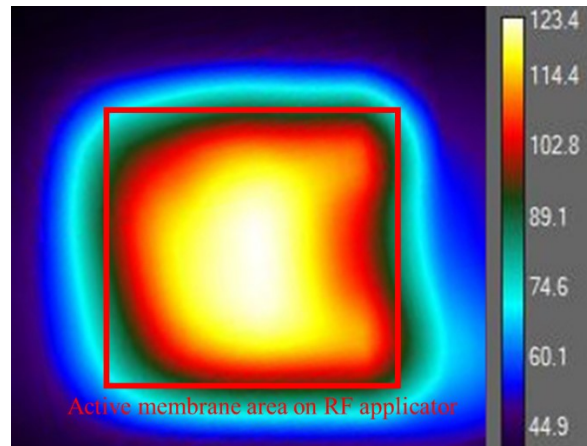


Figure S13. Sample thermal response captured by FLIR camera for PES-LIG-18 membrane with 91 MHz and amplifier gain 10%. The red boxed area is the exact location of the membrane on the RF applicator.

S15. RF input power observed at different amplifier gain settings.

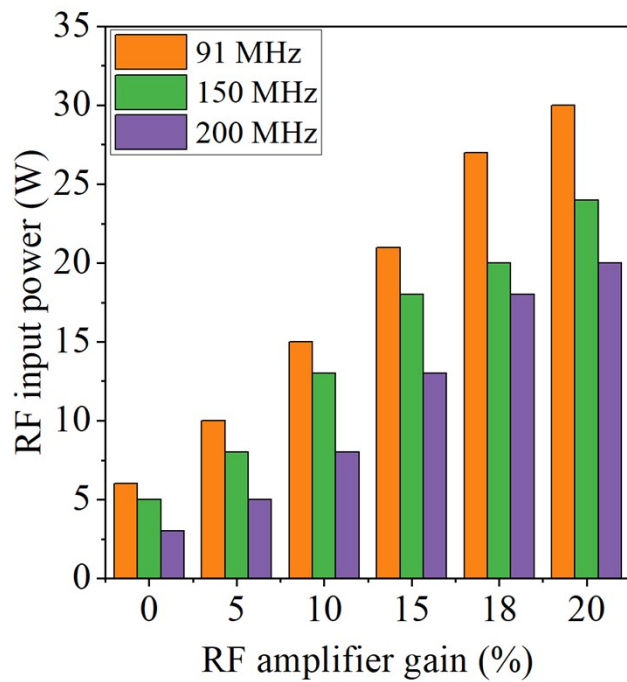


Figure S14. RF input power to PES-LIG membrane at different amplifier gains.

S16. Concept of conventional and surface heating in MD

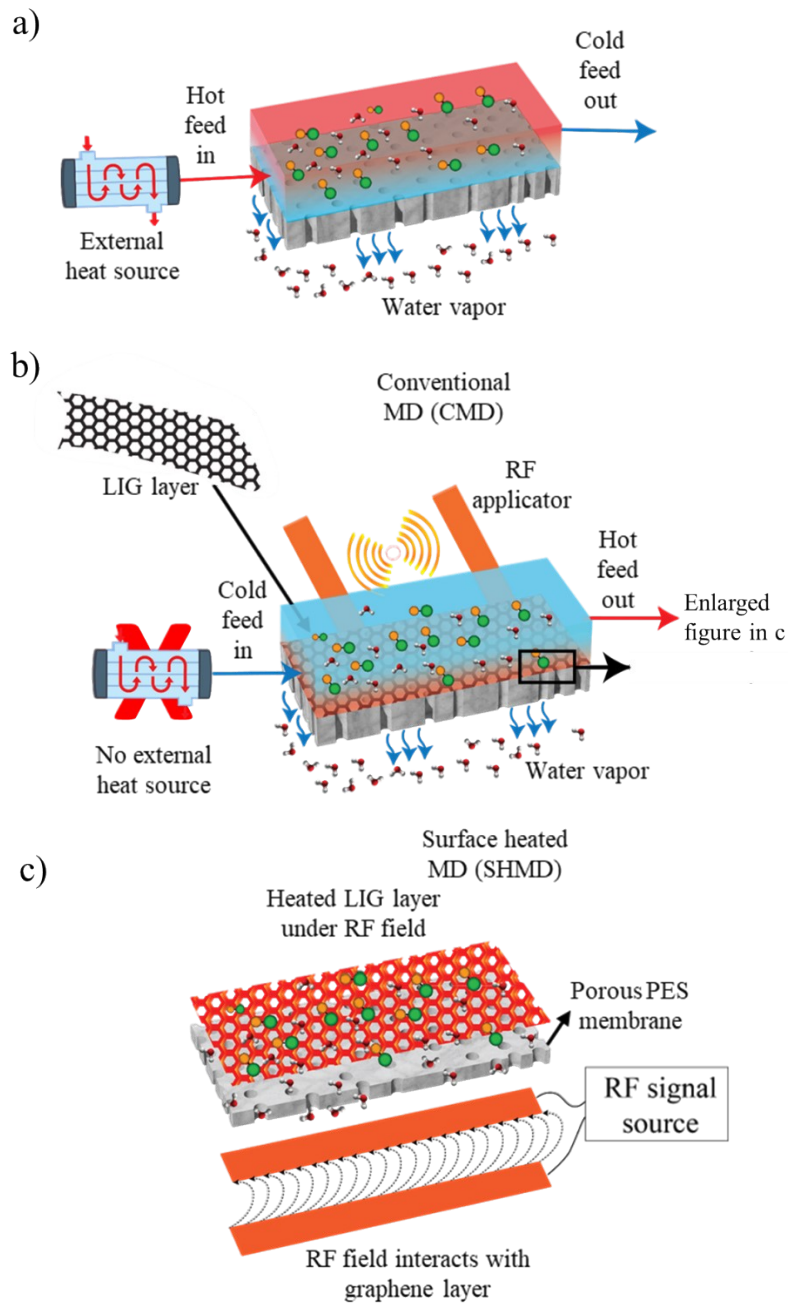


Figure S15: **a)** Schematic of conventional MD with external heating source and **b)** surface-heated MD concept with RF heating. **c)** Enlarged view of PES-LIG membrane surface interface with a sample RF applicator.

S17. Digital image of PES membrane

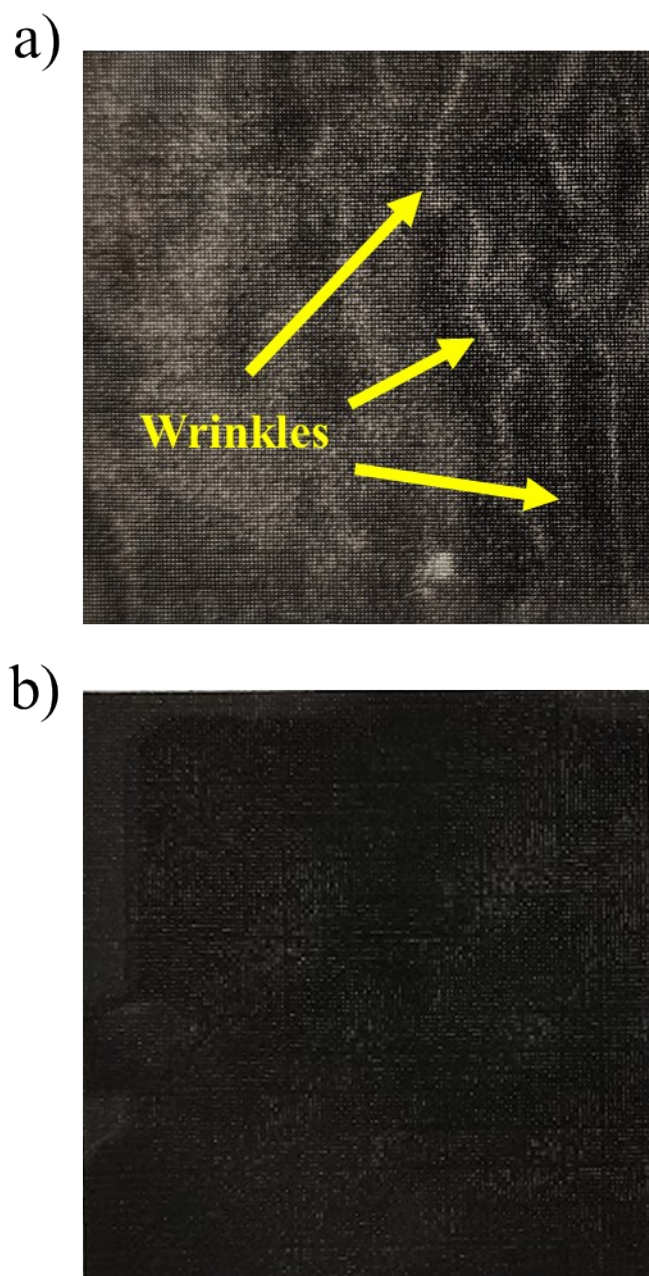


Figure S16. Digital image of a) PES-LIG-18 and b) PES-LIG-22 membranes.

S18. Effects of TP in MD

In conventional MD, as the water evaporates on the membrane surface, the latent heat of evaporation reduces the temperature of the liquid at the membrane feed interface.^[4] This results in lower interfacial temperature compared to the bulk feed temperature. This low temperature at interface decreases driving force of separation as low temperature decrease vapor pressure at the interface.^[5] Figure S9a shows a schematic of temperature profile of the conventional MD where at the feed side, the thermal boundary layer is formed due to evaporation. In addition to that, some heat is lost due to conduction through membrane material. Therefore, the membrane feed interface temperature T_{mf} is lower than bulk feed temperature T_{bf} . This makes the actual temperature difference across membrane $T_{mf} - T_p$, leading to decreased driving force known as TP effect.

In surface heating concept, bulk feed remains at ambient temperature and the membrane surface is heated which makes the feed membrane interface temperature higher than the bulk temperature.^[6] For this reason, TP effect does not play in surface-heated MD. Figure S9b shows the temperature profile for the surface-heated MD where temperature of feed within the boundary layer and feed membrane interface (T_{mf}) is higher than the bulk temperature (T_{bf}), resulting in higher driving force compared to conventional MD. This results in less energy requirement as only the feed liquid in the boundary layer of the feed membrane interface is heated.

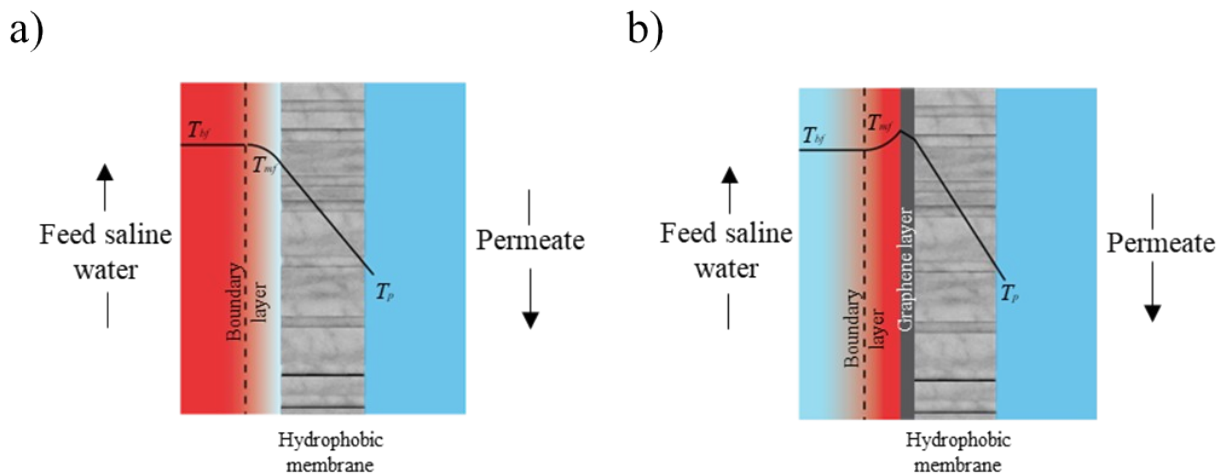


Figure S17. a) Temperature profile in MD cell for conventional MD vs. b) surface-heated MD.

Video S1. Laser ablation of PES substrate at 1% laser power.

Video S2. Laser ablation of PES substrate at 8% laser power.

References

- [1] Le, T.-S. D.; Phan, H.-P.; Kwon, S.; Park, S.; Jung, Y.; Min, J.; Chun, B. J.; Yoon, H.; Ko, S. H.; Kim, S.-W.; et al. Recent Advances in Laser-Induced Graphene: Mechanism, Fabrication, Properties, and Applications in Flexible Electronics. *Advanced Functional Materials* **2022**, *32* (48), 2205158. DOI: <https://doi.org/10.1002/adfm.202205158>.
- [2] Lin, J.; Peng, Z.; Liu, Y.; Ruiz-Zepeda, F.; Ye, R.; Samuel, E. L. G.; Yacaman, M. J.; Yakobson, B. I.; Tour, J. M. Laser-induced porous graphene films from commercial polymers. *Nature Communications* **2014**, *5* (1), 5714. DOI: 10.1038/ncomms6714.
- [3] Mahbub, H.; Saed, M. A.; Malmali, M. Pattern-Dependent Radio Frequency Heating of Laser-Induced Graphene Flexible Heaters. *ACS Applied Materials & Interfaces* **2023**, *15* (14), 18074-18086. DOI: 10.1021/acsami.3c00569.
- [4] Manawi, Y. M.; Khraisheh, M. A. M. M.; Fard, A. K.; Benyahia, F.; Adham, S. A predictive model for the assessment of the temperature polarization effect in direct contact membrane distillation desalination of high salinity feed. *Desalination* **2014**, *341*, 38-49. DOI: <https://doi.org/10.1016/j.desal.2014.02.028>.
- [5] Anvari, A.; Azimi Yancheshme, A.; Kekre, K. M.; Ronen, A. State-of-the-art methods for overcoming temperature polarization in membrane distillation process: A review. *Journal of Membrane Science* **2020**, *616*, 118413. DOI: <https://doi.org/10.1016/j.memsci.2020.118413>.
- [6] Razaqpur, A. G.; Wang, Y.; Liao, X.; Liao, Y.; Wang, R. Progress of photothermal membrane distillation for decentralized desalination: A review. *Water Research* **2021**, *201*, 117299. DOI: <https://doi.org/10.1016/j.watres.2021.117299>.